



# Acoustic Resonators for Intracellular Tagging

**Master Project @ Advanced NEMS Lab**

Rebecca C. Leghziel

Project realised under  
the supervision of  
Prof. Guillermo Villanueva  
as part of the  
MSc in Microengineering

**3 July 2020**

---

## **ABSTRACT**

Cell migration has always been essential for understanding the underlying mechanisms of physiological phenomena. For this reason, many diverse cell tracking methods are presented in literature, such as optical imaging, MRI and radionuclear imaging. However, optical methods are invasive and MRI and radionuclear imaging suffer from low spatial resolution. To overcome the limits imposed by state of the art cell tracking technologies, we propose to use plate acoustic wave resonators as a novel method for tagging single cells and tracking their spatio-temporal dynamics. In this work, we investigate and optimize the design of these tags, using finite element modelling simulations.

## **Acknowledgments**

I would like to thank Prof. Villanueva for his guidance, support and trust without which this project would have not been possible. I would also like to thank Muhammad Faizan, for providing me a finite element model of the device, on which I based the work presented in the report, and Soumya Yandrapalli, for sharing her knowledge on COMSOL multiphysics software.

# Contents

<b>1</b>	<b>Introduction</b>	<b>3</b>
<b>2</b>	<b>Acoustic Resonators for Cellular Tagging</b>	<b>6</b>
<b>3</b>	<b>Simulation Methods</b>	<b>7</b>
3.1	Simulation Parameters . . . . .	7
3.1.1	Geometry . . . . .	7
3.1.2	Materials . . . . .	8
3.1.3	Physics and Boundary Conditions . . . . .	8
3.1.4	Studies . . . . .	8
3.2	Definitions . . . . .	9
3.2.1	Electromechanical Coupling . . . . .	9
3.2.2	Quality Factor . . . . .	9
<b>4</b>	<b>Simulation Parameters Optimization</b>	<b>12</b>
4.1	Substrate Optimization . . . . .	12
4.1.1	Frame Geometry . . . . .	12
4.1.2	Substrate Material . . . . .	13
4.2	Mesh Optimization . . . . .	15
4.2.1	Definition of the Mesh . . . . .	16
4.2.2	Mesh Convergence using Modal Analysis . . . . .	16
4.2.3	Mesh Validation for Frequency Analysis Studies . . . . .	23
4.2.4	Quadrilateral vs Triangular Mesh Comparison . . . . .	24
<b>5</b>	<b>Conclusion</b>	<b>26</b>
<b>6</b>	<b>APPENDIX</b>	<b>30</b>
<b>A</b>	<b>Matlab Functions for Data Analysis</b>	<b>30</b>
A.1	Matlab function for data collection from COMSOL . . . . .	30
A.1.1	Function to open COMSOL file . . . . .	30
A.1.2	Function to organize the COMSOL file into a 2D cell . . . . .	30
A.1.3	Function to open a Table obtained from COMSOL . . . . .	31
A.2	Functions for Frequency Domain Studies . . . . .	32
A.2.1	Quality Factor . . . . .	32
A.2.2	Electromechanical Coupling . . . . .	33
A.3	QF from Modal Analysis . . . . .	34
A.3.1	Mode Identification . . . . .	34
A.3.2	QF Eigenfrequency for 3D Plots . . . . .	35

# 1 Introduction

Cell migration is essential for the maintenance and development of multicellular organisms and plays a major role in the evolution of physiological disorders, such as neurological diseases, cancer metastasis formation, fibrosis and many others. An understanding and investigation of cell migration, is therefore essential to understand the underlying mechanisms of physiological phenomena, which in turn are essential for successful intervention and the development of new drugs and cures [1].

Cellular tracking, has always played a central role in the field of biology. In fact, papers presenting cell tracking methods, date back to the early 20th century, where the main application was in embryological studies that aimed to understand how cells and tissues migrate to form an embryo. In 1934, *Nelson T. Spratt* placed finely powdered and purified carbon particles on epiblast cells of white leghorn chicks to track the movement of the epiblast cells in the blastocyst during early embryo formation [2]. Another common method for cell tracking at that time consisted in the use of China ink [3].

Nowadays, three main techniques are used to track and study the spatio-temporal dynamics in cells, namely: optical, magnetic resonance imaging (MRI) and radionuclear imaging. The operating principles, advantages and disadvantages for these three methods are summarised in Fig 1.

Optical techniques are the most commonly used because they are simple, quick and cost effective but limited to *in vitro* or very invasive *in vivo* applications. Optical tracking is achieved by means of fluorescent dyes and proteins, quantum dots or chemical reactions within cells that generate emission of photons (*bioluminescence*). Nevertheless, these optical techniques suffer from multiple disadvantages, such as the low spatial resolution of fluorescent dyes (few  $\mu\text{m}$ ), broad emission spectra, overlap of emission spectra with tissue autofluorescence, photostability, photobleaching etc. Some of these issues can be corrected using special algorithms for spectral unmixing [4], or by the use of filters to subtract tissue autofluorescence. However, the main unavoidable limitation remains the invasiveness of this technique [5][6].

On the contrary, MRI and radionuclear imaging are less invasive and are preferred for *in vivo* applications. When comparing the latter methods, MRI offers higher spatial resolution, speed and lower cost compared to radionuclear techniques [7]. With MRI, images can be acquired with a spatial resolution of  $50 \times 50 \times 50 \mu\text{m}$ . To enhance the contrast of target cells, superparamagnetic iron oxide (SPIO) nanoparticles are delivered inside the cells or are linked to the cell membrane. SPIO nanoparticles are 60-150 nm in diameter and formed by an iron oxide magnetic core, coated with *dextran* or *caboxydextran* to prevent nanoparticle aggregation. Furthermore, these SPIO nanoparticles are made of biodegradable iron, that might be re-used by cells in biochemical pathways for iron metabolism [5][8].

Due to the low spatial resolution of the aforementioned methods, in the past 10 years, new cell barcoding techniques have been developed and presented in literature to allow cells to be tracked on an individual level. For example, *Schubert et al* address this issue by using the lasing wavelength of *whispering gallery mode* microsphere resonators (with  $Q > 10^8$ ) as barcodes [9]; *Fernandes-Rosas et al* propose the use of microfabricated Poly-Silicon graphical barcodes, that can be identified under the mi-

croscope to tag cells [10][11]; *Rees et al* use 3 different colloidal quantum dots that correspond to 3 integer RGB values, to give cells a unique color ID in the RGB space [12]. Another approach makes use of genetic barcodes, consisting of an 8 base pair unique sequence, that can be used as identifier for individual cells. The advantage of this method is that it is possible to track cell lineages and fate, as the genetic barcode remains present throughout cell division [13]. Label free migration tracking methods have also been developed using computational models and tools for image processing [14][15][16].

Nevertheless, all these barcoding techniques are complementary to optical imaging or require RNA sequencing, therefore are just methods to enhance the resolution of invasive techniques.

A barcoding method suitable for minimally invasive *in vivo* applications is presented by *Hu et al*. In the paper they propose to wirelessly probe cells through electrical LC based RFID tags. Although this technique has many advantages, the low quality factor of LC frequency based tags (QF =1-5) might lead to cell misclassification and a loss in resolution [17].

Technique	Principles	Advantages	Disadvantages
<b>MRI</b>			
General aspects	(Super-)paramagnetic iron-oxide particles (for example, USPIOs) shorten T2 relaxation; lanthanides (for example, Gd) shorten T1 relaxation	Depth independence (allows whole-body-scanning); high spatial resolution; can be combined with traditional clinical imaging; no ionizing radiation	Relatively insensitive to tracers; contraindications (metal implants, claustrophobia); quantification can be challenging; limited availability
Ex vivo labeling	Contrast agent binds to or is internalized by target cells <i>ex vivo</i>	High labeling efficiency; high specificity (only cells of interest are labeled)	Need to isolate and manipulate cells <i>ex vivo</i>
In vivo labeling	Contrast agent is infused intravenously and binds to, or is internalized by, target cell <i>in vivo</i> ; target cell expresses contrast agent (transgenic approach)	No need to isolate cells	Lower labeling efficiency and lower specificity than <i>ex vivo</i> methods; toxicity issues related to intravenous injection; some <i>in vivo</i> methods require genetic manipulation of cells
<b>Optical</b>			
Fluorescence	Use of near-infrared dyes or quantum dots	No ionizing radiation; fast; histological detection performed <i>ex vivo</i>	Photobleaching (except quantum dots); limited depth penetration; limited spatial resolution compared with tomography
Bioluminescence	Emission of photons during energy-dependent reactions catalyzed by luciferase enzymes	Tracking over unlimited time; built-in 'viability indicator'; high signal-to-noise ratio; no ionizing radiation	Requires transfection of cells; limited spatial resolution and depth penetration; limited potential for clinical translation
Magneto-optical	Use of dual-modality probes that combine MRI-based and optical approaches	Allows whole-body scanning and combination of perioperative or intraoperative imaging; <i>ex vivo</i> histological detection possible	Contraindications (metal implants, claustrophobia)
<b>Radionuclear</b>			
SPECT	Gamma emitters (for example, $^{111}\text{In}$ , $^{99\text{m}}\text{Tc}$ )	Allows whole-body scanning; high sensitivity	Limited spatial resolution; ionizing radiation; quantification can be challenging
PET	Positron emitters (for example, $^{18}\text{F}$ , $^{64}\text{Cu}$ )	Allows whole-body scanning; high sensitivity; quantification feasible; no dilution of signal with cell division (transgenic approach)	Limited spatial resolution; requires genetic manipulation of cells; limited availability

Abbreviations: SPECT, single-photon emission CT; USPIO, ultra-small superparamagnetic iron oxide.

Figure 1: Working principles, advantages and disadvantages for different cell tracking methods [18].

To overcome the resolution limits caused by MRI and radionuclear imaging whilst allowing minimally invasive *in vivo* operation, we propose the use of high Q acoustic resonators for single cell tagging. The idea of using said devices, was first introduced in [19]. The advantages of this novel tagging technique are the possibility to operate *in vivo*, the high QF of the resonators and the low power requirements, as they don't need a threshold voltage to operate and the limit for the receivable signal depends just on the signal-to-noise ratio.

This project focuses on the design, using *Finite Element Modelling*, of these devices and can be broken into several aims:

- Scale down to cellular dimensions the FEM design of plate acoustic wave (PAW) resonators used for 5G filters
- find the optimal design parameters, to obtain a clean spurious-less admittance curve with high figure of merit
- Improve the accuracy of the FEM model, by exploring different meshing options
- Reduce model computation time to open the possibility for large data collection using multiple parametric sweeps
- create a work flow for data post processing in MATLAB

## 2 Acoustic Resonators for Cellular Tagging

In this project we use Plate Acoustic Wave (PAW) resonators as cellular tags. These devices, consist in a thin Lithium Niobate (LN) piezoelectric suspended membrane (400 nm thick), which is excited using an RF signal applied to interdigital transducer (IDT) electrodes that are deposited on top of the membrane. The RF signal generates an electric field that builds up in the piezoelectric material and drives the membrane into compression and expansion. Based on the applied frequency, the crystal cut and the in plane orientation of the device, it is possible to predominantly excite specific PAWs. PAWs can be categorized in LAMB Waves (S0, A0, S1, A1...) and Plate Shear Waves (SH0, SH1 ...) if they are excited in the longitudinal or shear direction [20] [21] [22][23][24].

These resonators are mainly used in ultra high band filtering applications, as they exhibit large electromechanical coupling ( $k_t$ ) and Quality Factor (QF) leading to high figure of merit ( $FoM = k_t^2 \cdot QF$ ), meaning low insertion loss and higher bandwidth [25].

Due to the high FoM, LN acoustic wave resonators are also a suitable option for cell RFID tags. The cell identification scheme is based on the resonance frequency, that can be tuned by changing the wavelength, defined lithographically by the pitch (i.e. the distance between two electrodes):

$$f = \frac{v}{\lambda} = \frac{v}{2 \cdot pitch}$$

where  $v$  is the phase velocity and  $\lambda$  is the wavelength. The phase velocity depends on the excited mode, in this project we focus on SH0 mode that has  $v \simeq 3500m/s$ . High FoM is desired for the this application, as the QF determines the frequency resolution that can be obtained and the  $k_t^2$  determines the bandwidth. Consequently the FoM, together with the resolution limits imposed by lithography, regulate the number of RFID tags that can be employed within the resonator bandwidth (Fig 2).

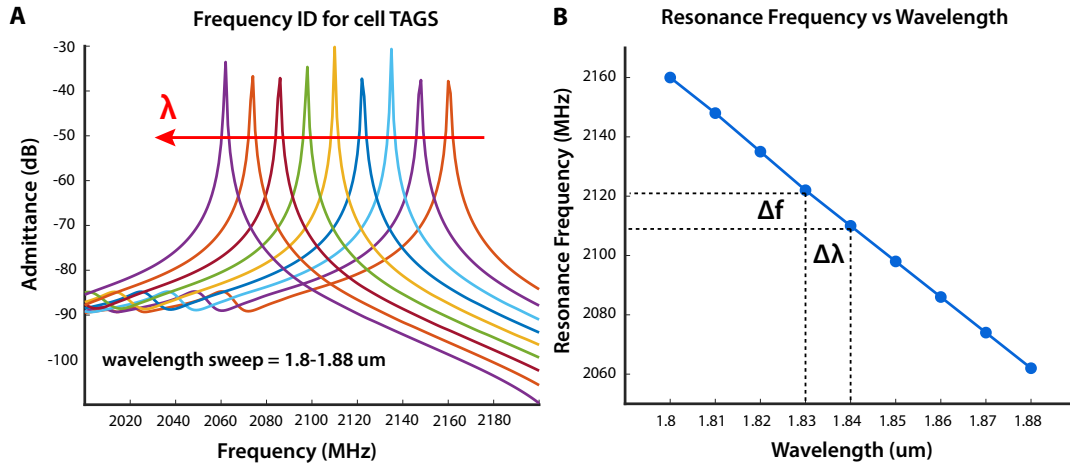


Figure 2: A) Frequency ID for cell Tags changed by sweeping the wavelength from  $1.8 \mu m$  to  $1.88 \mu m$  in steps of  $\Delta\lambda = 10nm$ , B) Resonance frequency change with wavelength, the minimum is limited by the QF while the minimum achievable  $\Delta\lambda$  is limited by the lithography resolution.

### 3 Simulation Methods

In this section, we present the parameters used to set up the finite element model for performing studies on SH0 mode acoustic cell tags. We then discuss the basic definitions that are representative of the device performance (i.e. QF,  $k_t^2$ ) and the different ways of computing them in MATLAB or directly in the COMSOL model.

#### 3.1 Simulation Parameters

Here, we briefly describe how the model was built in COMSOL, by going through the different sections in the model builder tree: geometry, materials, physics, boundary conditions and studies. Further information on the simulations can be found in [26][27].

##### 3.1.1 Geometry

The geometry used for all the simulations was optimized with parametric sweeps to obtain a combination of bus width (BW), gap and aperture that do not present in band spurious modes for  $\lambda = 2\mu m$ . SH0 resonator with three electrode fingers and two  $\lambda/4$  edge reflectors. The geometry, with the respective parameters for the main resonator body, is shown in Fig 3.

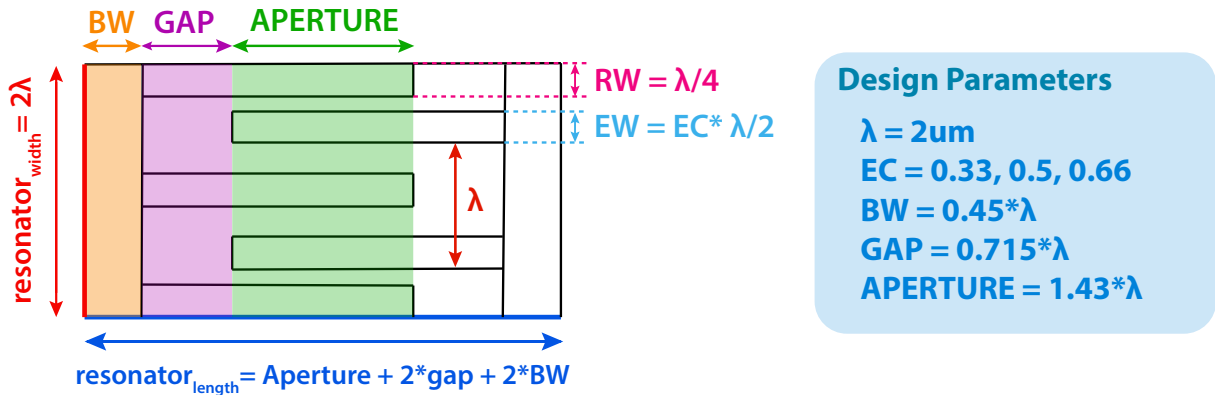


Figure 3: Geometry design and parameters for resonator main body

The thickness of the LN plate is set constant at 400 nm and the electrode thickness at 100 nm. The anchor dimensions were set to  $0.45\lambda$  in the width and  $0.8\lambda$  in the length, since they lead to the highest value of QF. The geometry design for the frame is discussed in section 4.1.1. The resonator main body is  $4\mu m \times 7.52\mu m$  and the minimum feature size is 250 nm in by the region between the reflector and electrode.



### 3.1.2 Materials

The simulations were performed using Lithium Niobate as the piezoelectric plate and Air or Aluminum for the IDT electrodes.

#### *Piezoelectric Plate*

LiNbO<sub>3</sub> is a highly anisotropic material. Based on the material cut and rotation angle with respect to the device axis, different excitation modes become predominant. In our simulations we focus on the shear SH<sub>0</sub> mode which is best excited on X-CUT LN, with the design rotated by 170° with respect to the Y-AXIS. The material parameters such as elasticity matrix, coupling matrix and relative permittivity used in this project were taken from a semester project report performed in Advanced NEMS laboratory on SH<sub>0</sub> excited devices [27]. These parameters were computed by an analytical model using euler rotation angles and matrix transformations.

#### *IDT electrodes*

Most of the simulations found in this report, were carried out using infinitely thin electrodes with no material assigned to them. This was done in order to avoid mechanical loading caused by the electrode material and consider only the electrical boundary condition on the IDT to obtain generalized results independent from electrode material. However, we also used Aluminium electrodes in our studies.

### 3.1.3 Physics and Boundary Conditions

As discussed in Section 2, the device converts an electrical signal into a mechanical deformation via a piezoelectric material. Therefore, the physics used to model the device are *Solid Mechanics* and *Electrostatics* which are coupled by the multiphysics *piezoelectric effect*.

There are two electrostatic boundary conditions, one is applied to the ground terminal, and the other is an harmonic perturbation of 5V applied to the positive terminal of the IDT electrodes. There is one boundary in the solid mechanics node, consisting of a fixed constraint applied to the border of the frame.

A perfectly matched layer (PML) definition is applied to the domain of the frame to attenuate the waves that leak from the anchors and to avoid spurious reflection from the substrate. The PML assumes that the substrate is infinite by absorbing all the outgoing wave energy that touch the PML region [28].

### 3.1.4 Studies

We used two types of studies: eigenfrequency and frequency domain studies.

The eigenfrequency studies are quicker and give results on QF and resonance frequency, although sometimes the mode shape can be hard to detect.

The frequency domain studies, on the contrary, take much longer computation time, depending on the

sampling frequency step used, but give a more comprehensive description of device parameters and overcome the mode identification issues, making the data post processing simpler. From the real and imaginary part of the admittance curve, we can extract the electromechanical coupling, QF, resonance frequency and information on spurious modes.

## 3.2 Definitions

In this section we discuss the basic definitions (i.e. Quality Factor, electromechanical coupling) that we use in the following sections of the report to characterize the performance of the device.

### 3.2.1 Electromechanical Coupling

The electromechanical coupling coefficient represents the efficiency in coupling electrical and mechanical energy and can be estimated as follows:

$$k_t^2 = \frac{\pi^2}{8} \frac{f_a^2 - f_r^2}{f_a^2} \quad (1)$$

where  $f_a$  and  $f_r$  are the antiresonance and resonance frequency. The MATLAB function to compute  $k_t^2$  for multiple parametric sweeps can be found in appendix A.2.2.

### 3.2.2 Quality Factor

The Quality factor (QF) is used as measure of the energy loss in electromechanical systems, and is defined as:

$$QF = 2\pi \cdot \frac{\text{Energy Stored}}{\text{Energy lost}} \quad (2)$$

The energy loss mechanisms that lower the value of QF are usually caused by material damping, viscous damping, thermoelastic damping and radiation of elastic waves at the anchor. For low frequency resonators the losses are usually dominated by viscous damping, while in high frequency resonators (MHz, GHz) the dominant loss mechanism is the radiation of energy through the anchors [28].

In the simulations performed in this project, we considered two main loss mechanisms:

1. *Anchor losses*: these are the main type of energy losses in high frequency resonators. The absorption of elastic waves in the PML domains cause damping in the structure. If no other losses are added to the COMSOL model, when computing the QF we are considering only the energy losses from the anchors and neglecting other losses.
2. *Material Losses*: these represent the ultimate limit of the achievable QF. For LN operating in our frequency range 1-5GHz, we consider isotropic material damping of  $1/Q=0.0002$  [20].

There are many other loss mechanisms that can be taken into account, such as viscous damping, losses from the IDT material, etc.

Since equation (5) cannot be used to calculate the QF for the PAW resonator, because it is difficult to assess the energy losses from the different damping contributions, we use three approximately equivalent methods from the frequency domain and the eigenfrequency studies.

### QF from Frequency Domain Study

We use two different methods to measure the Quality Factor from the frequency domain studies.

The **first method** consists in using the following definition of QF applied to the admittance plot:

$$QF = \frac{f_r}{\Delta f(-3dB)} \quad (3)$$

where  $f_r$  is the resonance frequency and  $\Delta f$  is the resonance width or the *Full Width Half Maximum* (FWHM), i.e. the bandwidth at which there is a 3dB drop in admittance from the resonance frequency. The code of the matlab function used to compute the Quality Factor can be found in Appendix B2. The sampling frequency needs to be chosen based on the QF and resonance frequency. We can generalize the sampling frequency as follows:

$$f_{sampling} = \frac{\Delta f(-3dB)}{N_{points}} = \frac{f_r}{N_{points} \cdot QF} \quad (4)$$

where  $N_{points}$  are the number of sampling data points within the FWHM bandwidth. To estimate  $N_{points}$  we performed a sweep of sampling frequencies (1MHz to 0.005 MHz) around the resonance frequency. Fig 4A shows the convergence of three resonator designs with different QFs. We observe that for all three designs, the QF converges at  $N_{points} \geq 7$ . Therefore, by knowing approximately the Quality Factor that we expect in the computation we set the sampling frequency to:

$$f_{sampling,max} \simeq \frac{f_r}{10 \cdot QF} \quad (5)$$

The **second method** consists in using COMSOL's built in expression *solid.Q\_freq* (i.e. Quality factor for frequency) that allows to plot Bode Q curves, as shown in Fig 4B, and the value at resonance frequency is taken as the QF. With this method, the Q-factor is calculated directly by COMSOL as "the number of cycles (at the given frequency) in which the total energy of the system decreases by a factor of  $e^{2\pi}$ "[29].

As shown in Fig 4C, the QF in this case is not affected by the sampling frequency. This method is advantageous to get an idea of the QF when performing coarse sweeps ( $f_{sampling} > 0.5\text{MHz}$ ) since there is no need of exporting the data to calculate the QF in Matlab as done when using equation (3).

### QF from Eigenfrequency study

In high quality MEMS resonators, the computation of QF can be done through the identification of the complex eigenvalue that is closest to the real-valued drive frequency that excites the resonant mode. By knowing the complex eigenfrequency  $\omega$ , the QF is calculated as:

$$QF = \frac{Re(\omega)}{2 \cdot Im(\omega)} \quad (6)$$

The real part of the complex eigenvalue is the resonance frequency while the complex part is indicative of all the energy loss mechanism. In general, real modes represent waves with zero net flux of energy across the system and are an approximation for mechanical systems where the damping is very low. On the contrary, when we have complex modes there is a net energy flux in the system (i.e. radiation of energy through anchors, coupling between fluid and mechanical structure, etc.)[28] [30]. Fig 4D, shows the SH0 mode and the eigenfrequency from which the QF is computed.

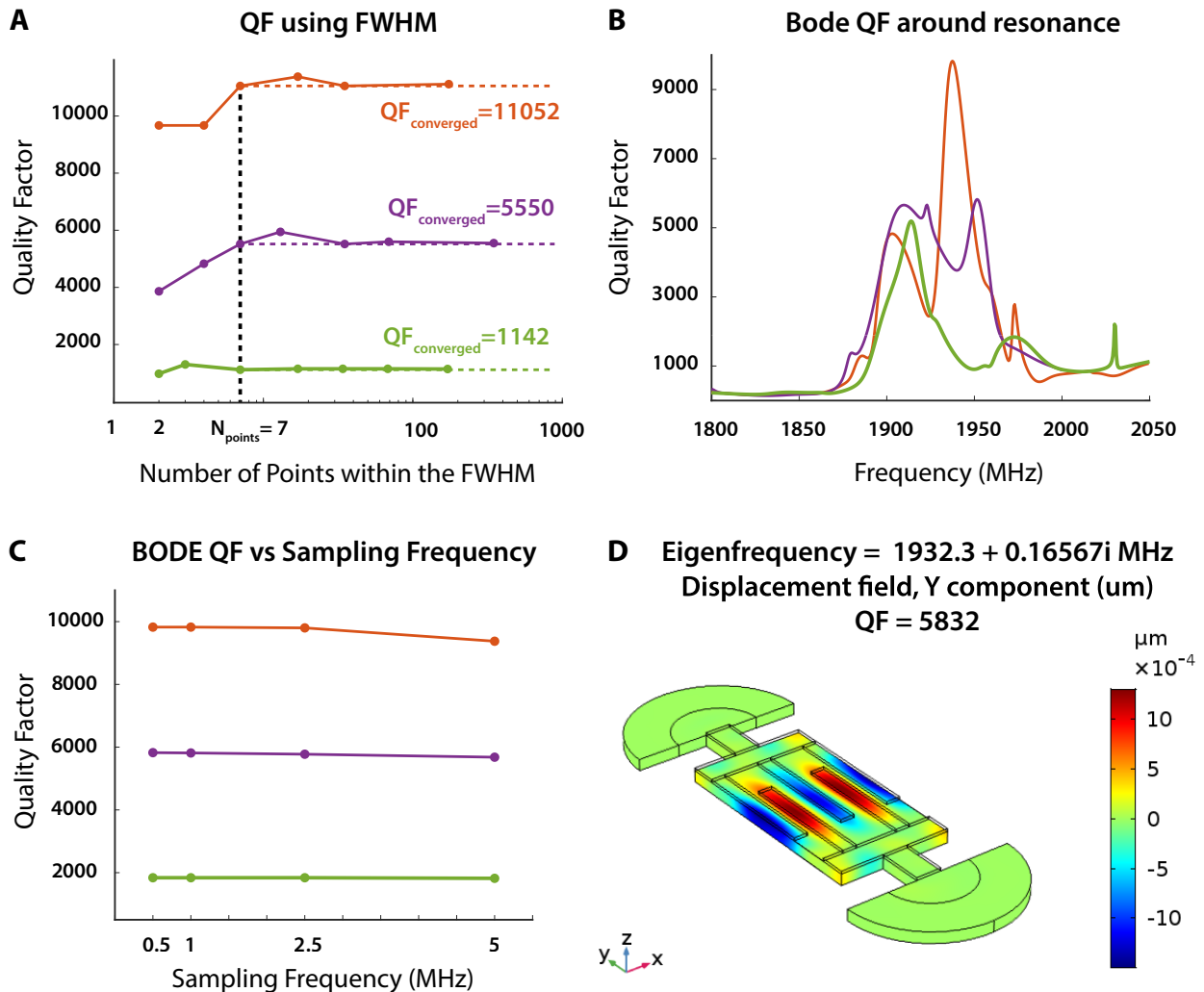


Figure 4: Comparison of methods for computing QF: A) Convergence of QF calculated using the FWHM formula for 3 different designs vs the number of sampling data points within the FWHM region. For all 3 designs the QF converge when we have at least 7 data points in the FWHM. B) Bode plot of QF vs frequency using the built in COMSOL function. C) Independence of Bode QF from sampling frequency. D) Example of QF calculated from modal analysis for the SH0 mode.

## 4 Simulation Parameters Optimization

In this chapter we tackle two of the main issues present in FEM models: **computation time** and **accuracy** of the results. The two are tightly linked to each other leading to a trade off. However, we show that by reducing the size of secondary geometrical parameters (i.e. the frame and substrate), we can reduce the computation time 3 fold, without affecting accuracy: we notice a maximum change in the QF by 3.4% in frequency domain studies, and a maximum change of 7.9% in eigenfrequency studies for the reduced geometry (4.1). Furthermore, by proposing a new structured mesh with quadrilateral element type, we improved the accuracy of the results without increasing computation time in the case of frequency domain studies, and reduced the computation time more than 2 fold in the case of eigenfrequency studies (4.2).

### 4.1 Substrate Optimization

The design of the frame in FEM modelling, should mimick as much as possible the substrate of the real device. A correct design of the frame is crucial, as it can affect the presence of in-band spurious modes. In fact, when waves impinge upon free edges, the reflected waves are a combination of all possible modes compatible with the given frequency [31]. To avoid this, we define a PML to absorb all the outgoing waves leaking from the anchors. In this section we first analyse how the geometry of the frame affects the quality factor and in band spurious modes (4.1.1). We then investigate the effect of materials and size of the substrate/PML interface (4.1.2).

#### 4.1.1 Frame Geometry

We compare two different frame geometries, that have been used in literature: cylindrical [30] and original [32]. The original frame geometry mimics the actual substrate, however it completely surrounds the main resonator body, causing the frame to occupy 85.95% of the entire geometry surface area. The cylindrical frame, on the contrary, is confined in the region of the anchors reducing the occupied surface area by the frame to 24.44% of the entire geometry.

Table 1 summarizes the obtained QF,  $f_r$ ,  $k_t^2$  and number of mesh elements for the original and cylindrical frame in two different scenarios: (1) with Aluminum IDT and (2) with infinitely thin IDT, with no material assigned. We notice that the QF calculated from **frequency domain studies**, show a 0.09% change between the original and cylindrical configuration when no material is assigned to the IDT, and a 3.4%

Table 1: Comparison of the QF obtained from frequency domain studies (QF(-3dB)) and eigenfrequency studies (QF( $\lambda$ )) for the different frame geometries for the design with Aluminum IDT and no material IDT

Design	QF(-3dB)	QF( $\lambda$ )	$k_t^2$	Mesh Elements
Original	6472	4643	22%	3958
Cylindrical	6478	4980	22%	1226
Original AI IDT	6421	2891	19.5%	3958
Cylindrical AI IDT	6650	2662	19.5%	1226

change in the case of Aluminum IDT. Fig 5A shows the admittance plot obtained in the four cases, we notice that the curves for cylindrical and original frame overlap and a frequency shift is present that is due to the mechanical loading by the Aluminum electrodes. Furthermore we see that in the case of Al IDT the electromechanical coupling,  $k_t^2$  is 22%, while for infinitely thin IDT the  $k_t^2$  is 19.5% in both frame configurations. When comparing the two frame design in the **eigenfrequency studies** (Fig 5B), we find a 6.8 % change in the case of infinitely thin IDT and an 7.9 % change in case of Al IDT.

In conclusion, there are no significant changes in the comparison between cylindrical and original frame, but there is a 3 times gain in computation time without affecting result accuracy using the cylindrical frame. For this reason, the cylindrical frame is preferred for simulations, especially when parametric sweeps, requiring long computation times, are performed. It can be noticed that the QF obtained by the frequency domain and by eigenfrequency studies are not in agreement. This issue is caused by the mesh and is addressed in section 4.2, here we just show that the results do not change for the different frame geometries within the same type of study.

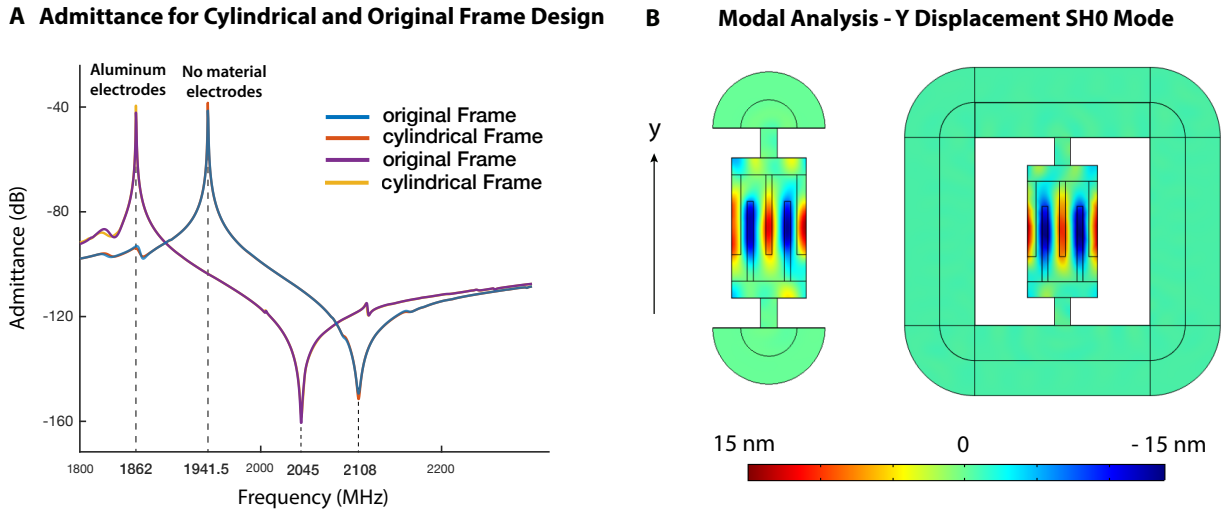


Figure 5: A) Frequency domain study for aluminum electrodes and no material electrodes for original and cylindrical frame configurations. B) Eigenfrequency domain study for cylindrical and original frame

#### 4.1.2 Substrate Material

To study the effect of the substrate on the QF and  $f_r$ , we consider two different substrate configurations, shown in Fig 6.

The first configuration, takes into account the wave travelling through the Silicon/Lithium Niobate interface on the substrate, before being absorbed in the PML, and is formed by 3 regions:

1. the first inner semi cylindrical region corresponds to the **undercut** generated during isotropic wet

etching of Silicon and it's radius is set constant at  $\lambda$

2. the middle semi cylindrical region, also called *inner substrate* in Fig 6A, mimics the **Lithium Niobate/Silicon interface** present in the substrate
3. the outer semi cylindrical region is the **PML**

The second substrate geometrical configuration, shown in Fig 6B, neglects the LN/Si interface and the waves leaking into the substrate travel through the undercut region and then are directly absorbed into the PML. This configuration is favorable for computation time, as we reduce the substrate and consequently the number of elements.

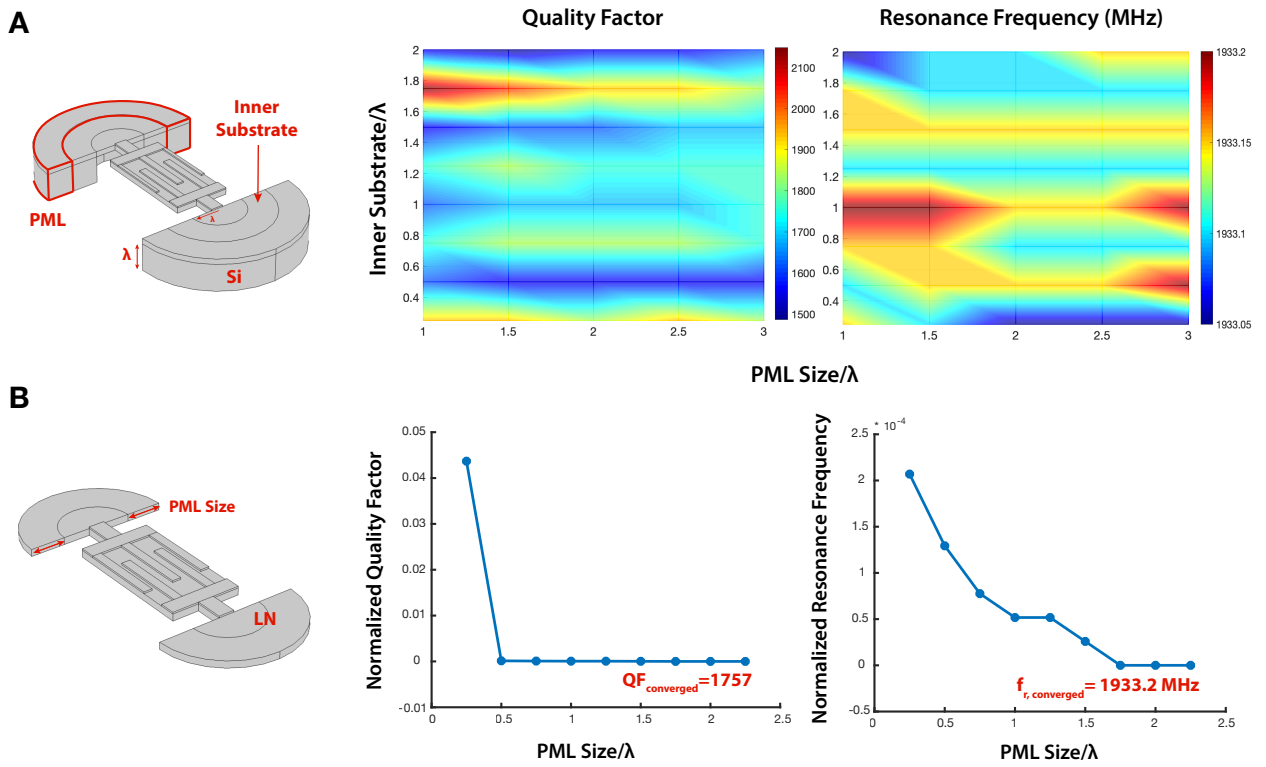


Figure 6: Comparison of two substrate designs: A) QF and resonance frequency results obtained for frame geometry taking into account the LN/Silicon interface B) QF and resonance frequency results obtained for reduced frame geometry.

In the case of the design with the Si/LN interface, we swept the radius of PML from  $\lambda$  to  $3\lambda$  in steps of  $0.5\lambda$ . The inner substrate, was also swept from  $0.25\lambda$  to  $2\lambda$  in steps of  $0.25\lambda$ . We notice that the QF varies between 1500 to 2000 for different inner substrate dimensions with a periodicity of  $\frac{\lambda}{2}$ . The same periodicity is observed in the resonance frequency. We notice that the QF and  $f_r$  fluctuations represent a maximum change in the results of 25% in the QF and 77.6 ppm in resonance frequency. Furthermore, as expected, the QF and  $f_r$  are minimally affected by the dimensions of the PML (Fig 6A).

In the second design, that neglects the Si/LN interface, we changed the PML size from  $0.25\lambda$  to  $2.25\lambda$  in steps of  $0.25\lambda$ . We notice that the QF converges to 1757 for PML Size  $> 0.5\lambda$  and the  $f_r$  converges to 1933.2 MHz for values greater than  $1.75\lambda$ .

Since the converged value for the design in Fig 6B is within the fluctuations in QF and  $f_r$  present in design of Fig 6A, we use the second design for all following simulations, as no major change is brought by the addition of the Si/LN interface, other than a increase in the computation time. Furthermore, since the fluctuation present in the first design are negligible, we can conclude that by using the second design, it is possible to obtain similar results with a maximum error of 16% in QF and 78 ppm in the  $f_r$ , depending on the chosen size of the inner substrate that we compare with.

It should be noted that all results were obtained from frequency domain studies and using a triangular mesh structure on the LN substrate.

## 4.2 Mesh Optimization

The mesh plays a significant role on the accuracy of the results obtained from FEM simulations, as it determines how the model is solved. When building a mesh, we change the shape, element type, size, density, number of elements and element quality. These element parameters, in turn affect the computation time and amount of memory needed, how the solution is interpolated between nodes, and the accuracy of the final solution [33].

COMSOL multiphysics software provides different meshing options to manually define the mesh, as well as a *physics generated mesh* which is automatically determined based on the device physics inputted by the user. A previous semester project, conducted in Advanced NEMS laboratory, compared the physics generated mesh with a new structured mesh which was manually determined by convergence studies. It was shown that by using a structured mesh, which is triangular on the  $LiNbO_3$  substrate and quadrilateral on the IDT, the error reduced 2.5 fold in the frequency and 8 fold in the QF, compared to the physics generated mesh. However, this study focused on a specific geometry of a 9 electrodes S0 excited device with wavelength  $12\ \mu\text{m}$ . We noticed that when using this mesh on a  $\lambda = 2\ \mu\text{m}$  SH0 excited device with 5 electrodes, the QF doesn't show consistent results between modal and frequency domain analysis [26].

To solve this issue, we propose a new partitioned mesh structure that is quadrilateral on the LN substrate as well as on the electrodes and anchors, and assign different number of elements (i.e. element size) in different regions of the partitioned LN substrate as described in 4.3.1.

In this section we first describe how the device was partitioned and how the quadrilateral mesh was defined (4.3.1). We then show mesh convergence studies using modal analysis (4.3.2) and validate the mesh by comparing the QF and frequency results obtained in frequency domain analysis(4.3.3). Finally, we compare the new quadrilateral partitioned mesh with the triangular mesh previously established in the laboratory for larger devices (4.3.4).



### 4.2.1 Definition of the Mesh

To obtain a mesh with different element size in the different regions of the Lithium niobate substrate we partitioned the geometry in 54 blocks. The geometrical blocks are defined using parametric values, such that when the geometry is changed, the width and length of each block changes accordingly. For each of these blocks, we assigned a different number of elements on the edges in the x and y direction based on the convergence studies performed in section 4.3.2 and used *mapped distributions* to interpolate the lines and obtain quadrilateral elements. Fig 4 shows the edges where the number of elements are defined and each edge correspond to a specific geometrical parameters of the device (i.e. bus, gap, aperture etc.). The mesh on the frame, including the PML and undercut region, were built differently, by defining the element size as a function of the wavelength. Furthermore we applied a triangular mesh in the undercut region as a quadrilateral mesh would have caused a high distortion of the elements. The mesh defined on the Lithium Niobate (PML, undercut, anchors and main body) is swept through the thickness direction (2 layers) and electrodes (1 layer).

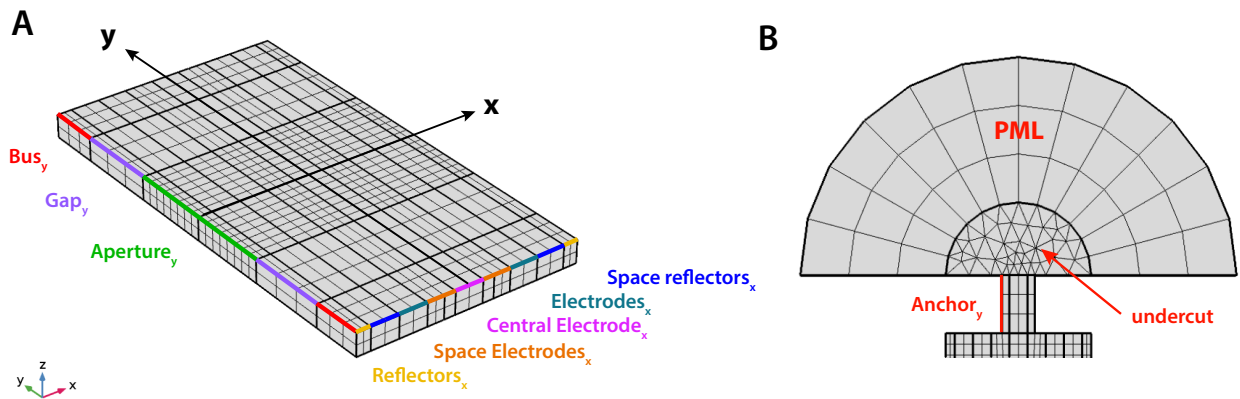


Figure 7: A) Partitioning of the LN main body into 54 blocks with the number of elements defined on the edges of each block. B) Mesh for frame region and anchor.

### 4.2.2 Mesh Convergence using Modal Analysis

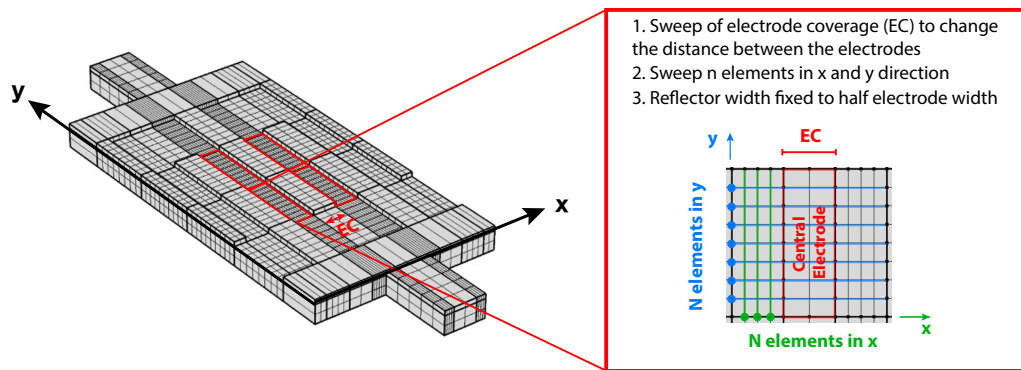
Mesh convergence was obtained by changing the number of elements in each of the block edges on the LN substrate to reduce the element size. We split the convergence studies in the x and y direction edges and in the case of the region between the electrodes we change the element size in both directions at the same time. All convergence studies found in this chapter were performed using Modal Analysis.

#### Mesh convergence in x direction

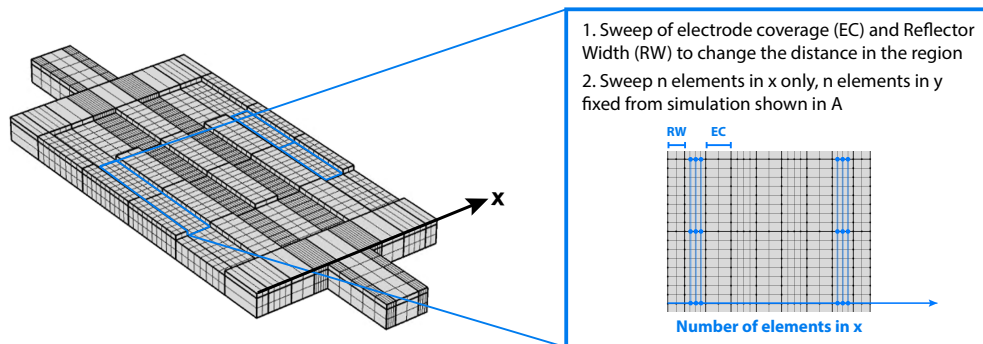
The methods for mesh convergence studies in the x direction can be found in Fig 8. We start by increasing the number of elements on the geometrical blocks corresponding to the LN space between the electrodes on the x and y edges simultaneously for different electrode coverages (EC) (Fig 8A).

We then fix the number of elements in  $y$ , obtained from the latter simulation, and sweep the number of elements in the  $x$  direction for the region between the reflectors and electrodes for different ECs and reflector widths (RW) (Fig 8B). We distinguish between the LN region between reflector-electrode and electrode-electrode, as we use different reflector widths, leading to smaller regions between the reflector and electrode. We finally, do a last simulation in  $x$  direction for the number of elements on the central finger, the electrodes and reflectors for different EC and RW (Fig 8C). In this case we distinguish the central electrode from the other electrodes, since the mesh on this electrode affects also the element size on the anchors.

**A Simulation to determine number of elements in the region between electrodes in  $x$  and  $y$  direction**



**B Simulation to determine number of elements in the region between reflectors and electrodes in  $x$**



**C Simulation to determine number of elements on the Interdigital Transducer in the  $x$  direction**

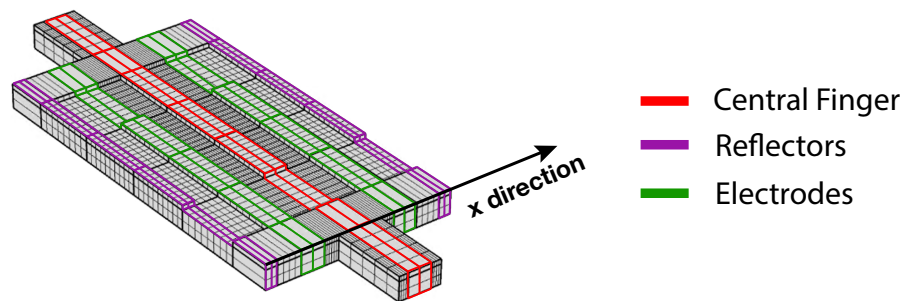


Figure 8: Simulation methods for convergence studies in the  $x$  direction using Modal Analysis

### A. Regions between Electrodes

To determine the mesh in the region between the electrodes, we swept the number of elements in the x (NEx) and y (NEy) direction simultaneously for electrode coverages of 0.33, 0.5 and 0.66, as described in Fig 8A. The mesh convergence study results are shown in Fig 10A, where the converged regions are contained within the blue dashed line.

From these heat plots, we notice that the QF is mainly affected by the mesh defined in the y direction (i.e. in the aperture region) for  $EC \leq 0.5$ . In fact, for  $EC \leq 0.5$ , we find that within the converged region, defined at  $NEy > 7$  and  $NEx \geq 2$ , the maximum percentage error for QF is 1.3% for  $EC=0.33$  and 4.8% for  $EC=0.5$ . Out of the convergence region, we find a maximum error of 15.9% for  $EC=0.33$  and 30.9% for  $EC=0.5$  for QF. Since the maximum error in QF out of convergence is much greater than the error obtained in the resonance frequency (less than 250 ppm for  $EC \leq 0.5$ ), we choose the number of elements based on the converged results for QF.

For  $EC=0.66$ , the number of elements needs to be increased 1.5 fold in the x direction ( $NEx=8$ ) and 2 fold in the y direction ( $NEy=12$ ) to obtain a converged value, as shown in Fig 9. Within the converged re-

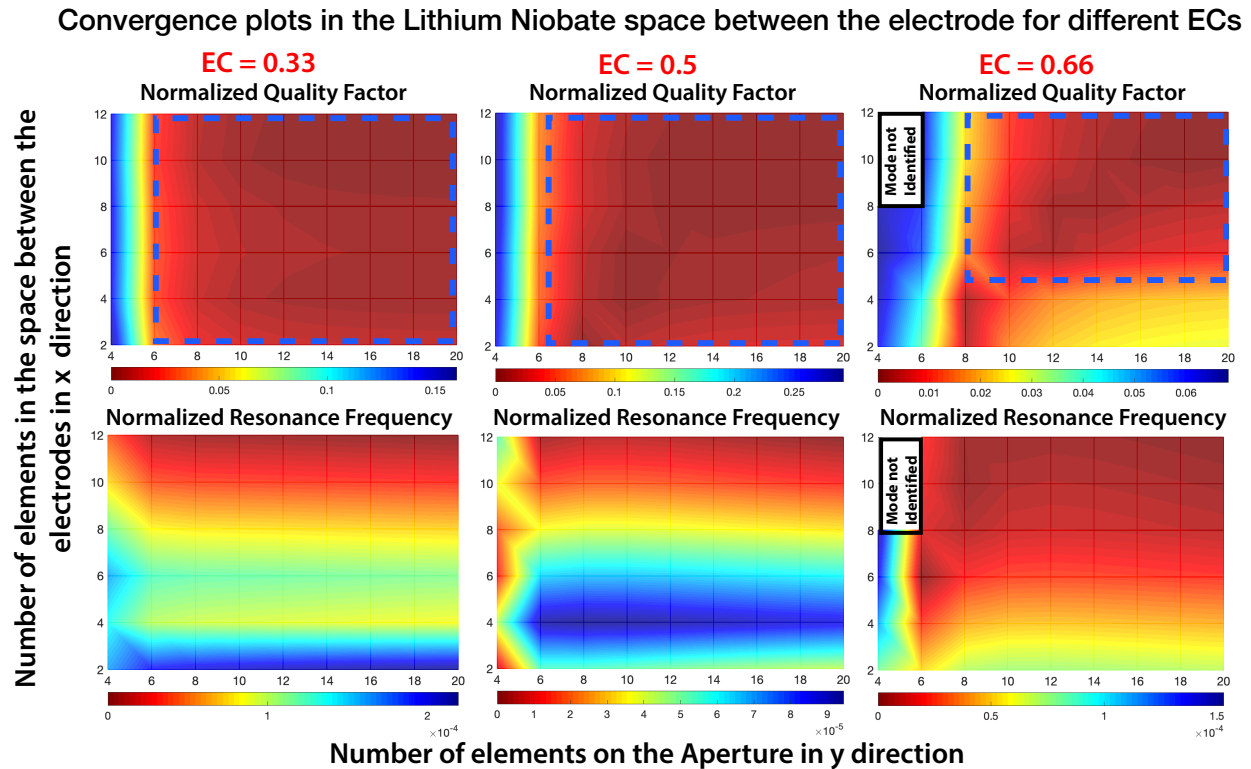


Figure 9: Convergence plots of QF and resonance frequency for the LN space between electrodes using different electrode coverages

Table 2: Mesh in the region between electrodes for  $EC \leq 0.5$  and  $EC > 0.5$

EC	NEx (Space)	NEy (Aperture)
$EC \leq 0.5$	3	8
$EC > 0.5$	8	12

gion we obtain a maximum change of 1% in QF while outside convergence 9.32%. Moreover, we notice that when  $NEx > 8$  the mode shape isn't clear and cannot be identified. This implies that the cleanliness of the mode shape is dependent on the number of elements in the mesh. Due to the different NE needed for convergence depending on the EC, we define two meshes for  $EC \leq 0.5$  and  $EC > 0.5$  in this region as shown in Table 2.

### B. Regions between the Reflector and Electrode

Fig 10B shows the results obtained for convergence studies in the region between the reflectors and the first electrode corresponding to Fig 8B. To change the width of the region, we performed parametric sweeps on the EC(0.33, 0.5, 0.66) and Reflector Width ( $\lambda/4$ ,  $\lambda/6$ ,  $\lambda/8$ ,  $\lambda/10$ ). The results for QF and  $f_r$  are normalized as the relative error between the result for a specific number of elements and the finest mesh resolution result which is assumed to be the converged value.

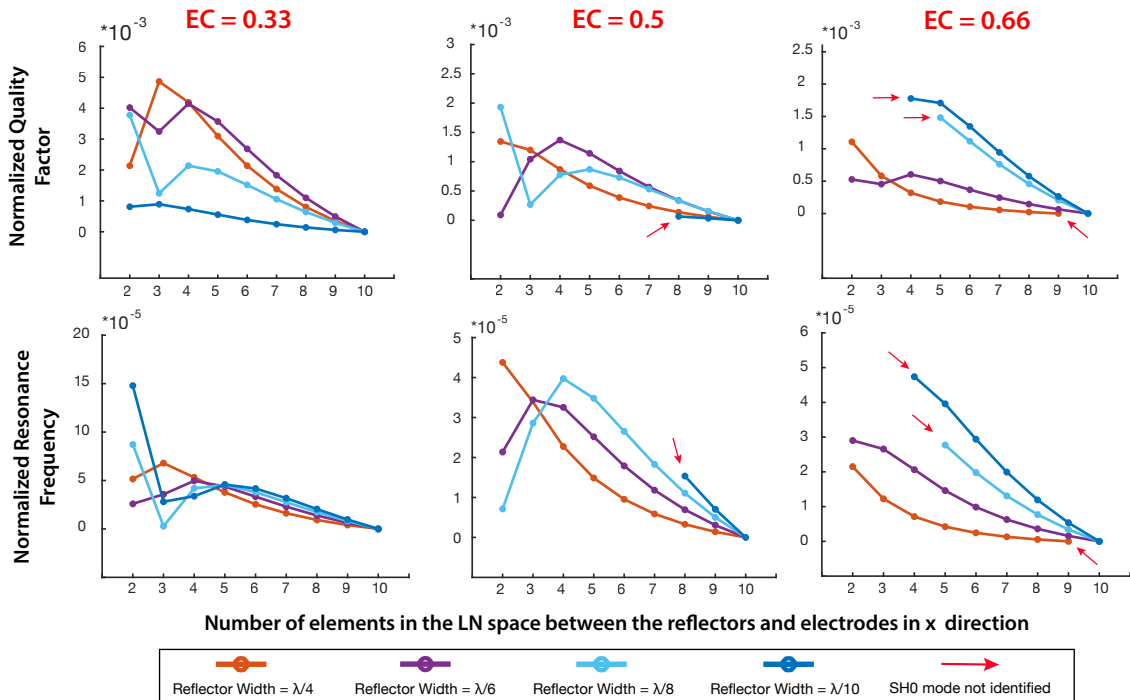


Figure 10: Normalized QF and  $f_r$  for the region between reflectors and electrode for different electrode coverages and reflector widths.

We notice that for all reflector widths and electrode coverages, the error is below 0.5% for Quality Factor and 1.5 ppm for resonance frequency. The low error might be caused by the fact that the number of elements in the y direction (aperture) was established in the simulation in A and the space between reflectors is mainly affected by the number of elements in y and independent from x. Since the error changes are minute, we choose the lowest number of elements to increase computation efficiency. Furthermore we notice from Fig 10B that not all modes were successfully identified for EC =0.5 and 0.66. However by increasing the number of elements the mode became clearer.

### **C. Fingers and Reflectors**

The number of elements in the electrodes and reflectors were swept from 1 to 10 and the results are shown in Fig 11. We notice that we obtain converged results for NEx= 2 elements for all the electrodes and reflectors.

Fig 11A shows the QF and resonance frequency convergence for the **reflectors**. We notice that for reflector widths of  $\lambda/10$  and  $\lambda/8$  the error is below 0.1% for 1 element in x. However as the reflector width increases to  $\lambda/6$  the error increases to 5% for 1 element in x. For all reflector widths, we notice that for NEx=2 the maximum error in the QF is 1.6% and in the resonance frequency is 7 ppm. Hence, NEx =2 is chosen as converged value for simulations.

Fig 11B shows the QF and resonance frequency convergence for the **central finger** for EC of 0.33, 0.5 and 0.66. For all ECs we notice that for NEx=2, the error is below 2% for the QF and 9ppm for the resonance frequency. Furthermore we notice that for NEx =3 we the mode shape is not clear and hard to identify using the algorithm in appendix A.3 for all ECs. In order to have a converged mesh for all EC we choose NEx =2.

Fig 11C shows the convergence plots for the **electrodes**. Also in this case, for all electrode coverages the QF and  $f_r$  converge for NEx = 2 with an error in QF below 1% and below 2ppm in the  $f_r$ . When passing from NEx = 1 to NEx = 2, the error decreases from 16% to 1% in the case of EC=0.66, from 6% to 0.2% for EC=0.5 and from 0.008% to 0.002% in the case of EC=0.33, showing that the number of elements required in this region is dependent on the electrode width. We choose NEx=2 to minimize the error for different ECs.

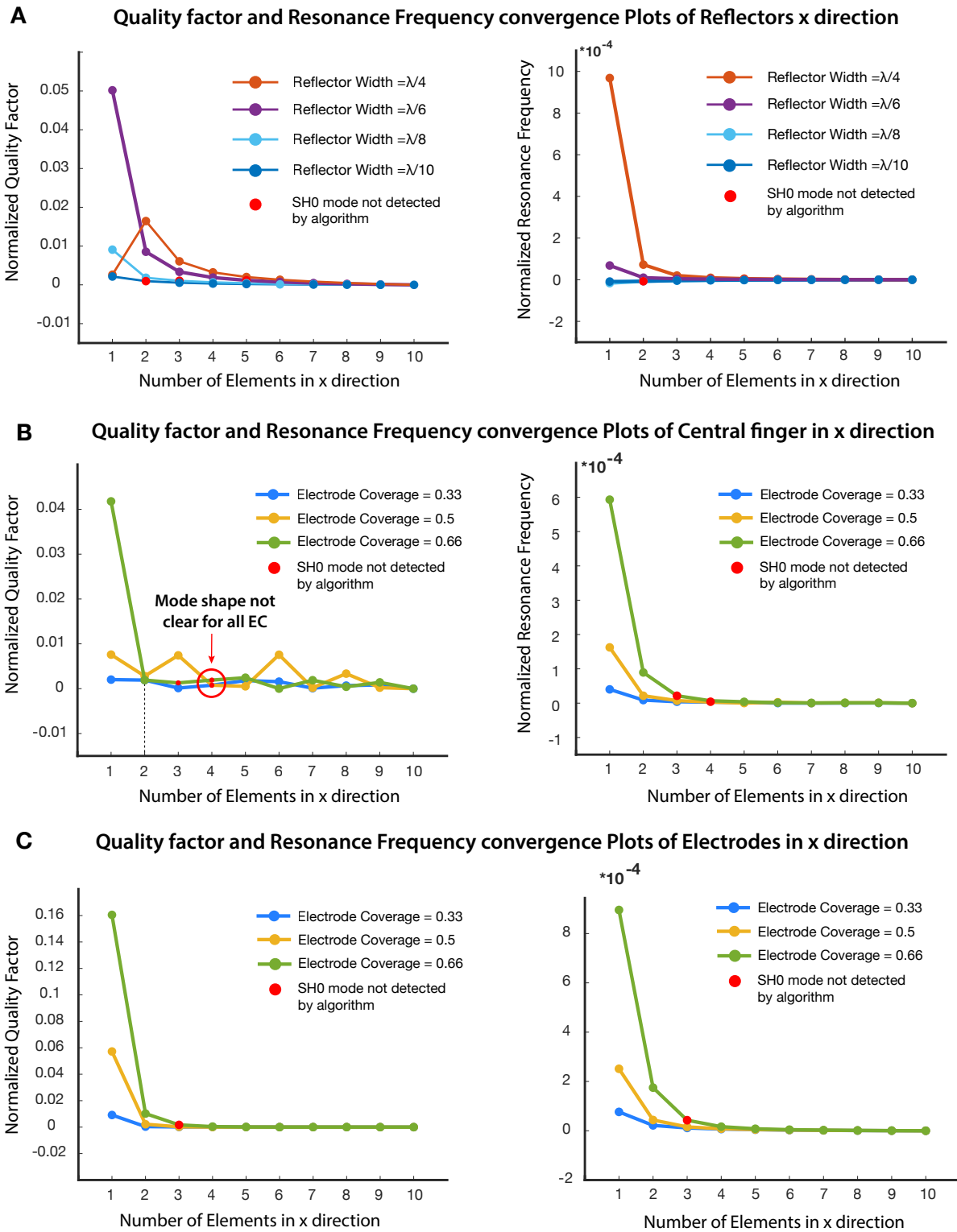


Figure 11: QF and  $f_r$  results in x direction for A) reflectors, B) central finger and C) electrodes.

## Mesh Convergence in the Y direction

### Bus, Gap and Anchors

We swept the number of elements in the y direction ( $NE_y$ ) in the regions of the bus, gap and anchor as shown in Fig 12A. We notice that we get the largest variation in error in the gap region, where the QF increases up to 4.5 times higher values than the converged one at  $NE_y=2$ . As the number of elements increases to  $NE_y = 5$  the error in QF decreases to 8.5%. The Bus and Anchor show a lower error compared to gap. For  $NE_y = 3$  the error in the QF for the bus is 10.8% and for the anchor 0.3%. In conclusion we choose as converged mesh,  $NE_y=3$  for bus and anchor, and  $NE_y = 5$  for the gap with a maximum error of 8.5% in QF given by the gap convergence.

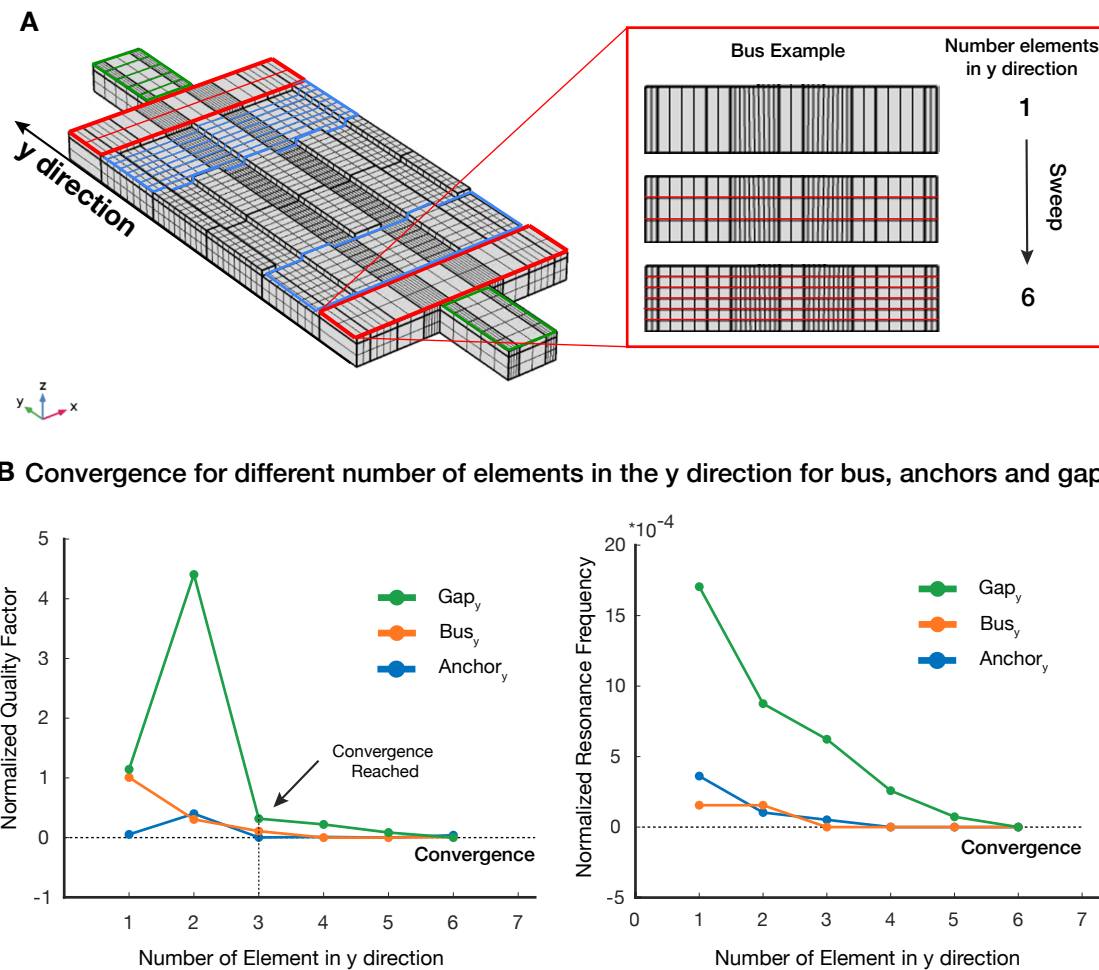


Figure 12: A) Simulation methods for anchor, gap and bus region in the y direction, B) Convergence results for QF and  $f_r$ .

### Frame: PML and undercut

The convergence studies for the PML and undercut in the frame were performed by changing directly the element size rather than the number of elements as shown in Fig 13A. The obtained results are shown in Fig 13B. We see that in the undercut region, the error decreases from 8% to 0.2% when passing from element size of  $\lambda$  to  $0.4\lambda$  while the resonance frequency error remains stable. For the PML region, we reach convergence for larger element size: for element size of  $0.9\lambda$  the error in QF is 1.2% and the error in resonance frequency is below 100 ppm.

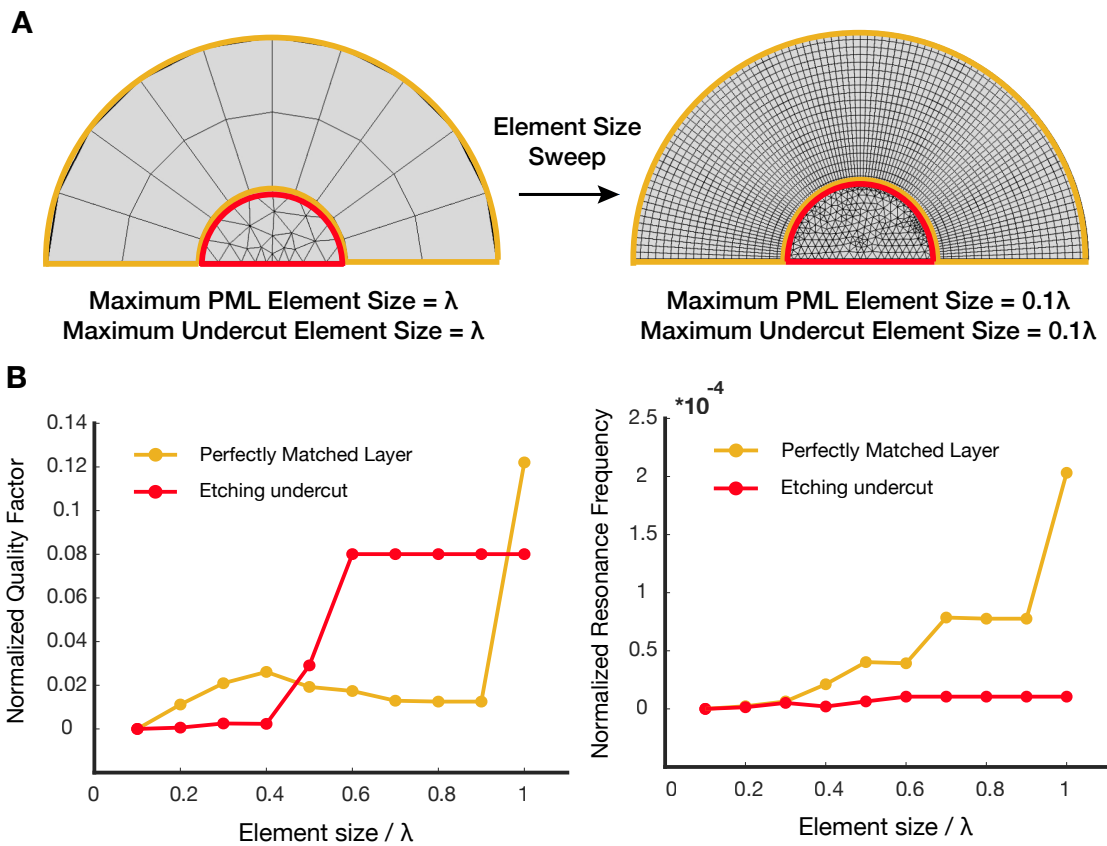


Figure 13: A) Simulation methods for decreasing element size in the frame region, B) QF and  $f_r$  results for the the PML and undercut region.

### 4.2.3 Mesh Validation for Frequency Analysis Studies

From the previous section (4.2.2) we obtained a converged mesh for eigenfrequency studies. The same procedure should be performed to get an optimized mesh for studies in the frequency domain. However, since we already know the converged value for QF (from the modal convergence studies), we can validate the same mesh for the frequency domain, by comparing the obtained QF results from the two different studies.



We computed the QF from the frequency domain studies using the FWHM definition for 9 different designs. For each design we calculated the percentage relative error between the QF(-3dB) and the converged QF obtained in eigenfrequency studies. Fig 14 shows the % error as a function of QF of 9 different designs. We notice that as the QF decreases, the error increases exponentially with the maximum observed error being 21% for a QF = 743. Furthermore, for 9 different QF values we obtain an average error of 9%. Since the average error is below 10% we can assume that this mesh can be used also in frequency domain studies.

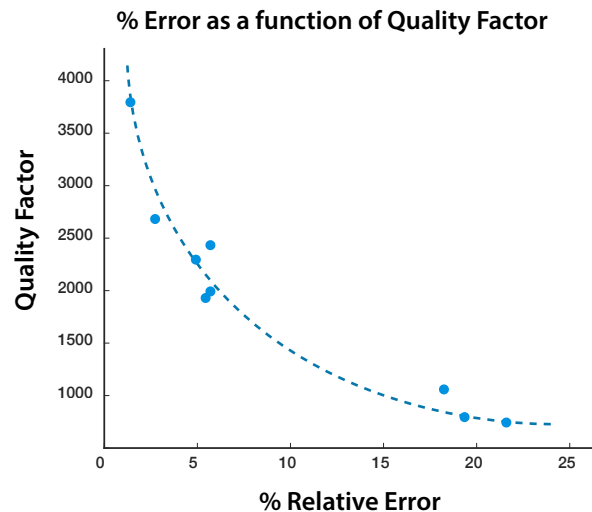


Figure 14: Exponential dependence of the error with respect to the Quality Factor.

#### 4.2.4 Quadrilateral vs Triangular Mesh Comparison

Here we compare the triangular mesh, that was previously used in the lab, with the new quadrilateral mesh. From Table 3, we see that when we pass from triangular to quadrilateral element type, the number of elements decreases 2.3 times for the mesh used in modal analysis and doesn't change for the mesh used in frequency domain studies. Furthermore, we notice that the average element quality increases from 0.87-0.88 to 0.96. In Fig 15 we observe that in triangular mesh the element quality is the lowest, in the region between the electrodes where it reaches a minimum element quality of 0.45, while in the case of quadrilateral mesh the element quality is 1 everywhere on the resonator body and reaches a minimum of 0.55 on the frame undercut region, where a triangular mesh is used.

Moreover, we assessed the accuracy of the results obtained with the two mesh types, by comparing the QF values obtained in eigenfrequency and frequency domain studies. We noticed that in the triangular mesh we obtained a maximum relative error of 55% for a specific design combination and have an average error of 24% over 9 different designs. For the quadrilateral mesh we obtain a maximum error of 21% and an average error of 9% over the same 9 designs. We can therefore conclude that we see an improvement in accuracy and a reduction in computation time using the quadrilateral mesh.

Table 3: Comparison between Quadrilateral and Triangular mesh

Mesh Type	Number of Elements ( $\lambda$ )	Average Element Quality ( $\lambda$ )	Number of Elements (f)	Average Element Quality (f)
Quadrilateral	2086	0.96	2086	0.96
Triangular	4901	0.88	1996	0.87

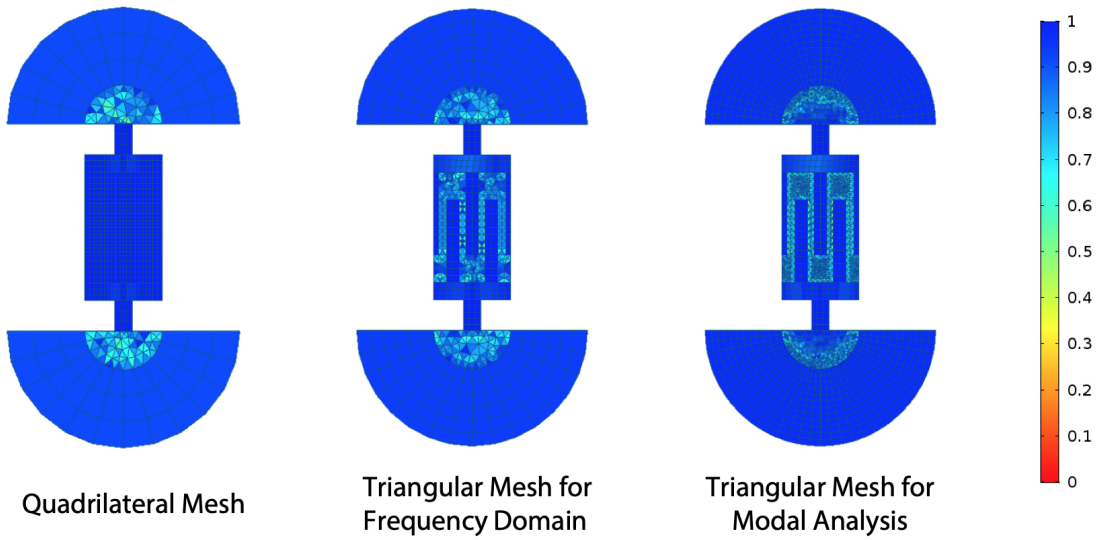


Figure 15: Comparison of mesh quality for the quadrilateral and triangular meshes used

## 5 Conclusion

The project focused on the optimization of FEM model for 3 finger LN excited PAW resonators. We first have found a combination of geometrical parameters, which was not showing in band spurious modes. We then have proven that by reducing the frame region, it is possible to improve computation time 3 fold, without affecting the accuracy of the results with an observed maximum change in QF of 3.4%. We have additionally proven, that there is no significant difference by adding a LN/Silicon interface in the substrate, as present in the real device, and computation time can be reduced by just defining a PML after the undercut region. Moreover, we have improved the average mesh element quality from 0.87 to 0.96 and reduced the computation time 2 fold for modal studies, by using a quadrilateral structured mesh. The proposed mesh shows a maximum error of 20% for low QF values ( $QF < 1000$ ) and an average error of 9% when comparing the QF between modal and frequency domain studies. Furthermore we observed a 2 fold improvement in accuracy compared to a triangular mesh previously used in the laboratory.

In this project we also propose a work flow, for analysing the data obtained in COMSOL for large parametric sweeps by using matlab functions to open, order and consequently compute QF and  $k_t^2$  from raw data text files obtained in COMSOL (appendix).

By optimizing the computation time and accuracy, and automatizing the calculation of QF, resonance frequency and electromechanical coupling, in frequency domain and eigenfrequency studies for multiple parametric sweeps, we have paved the way for more reliable and faster data collection and analysis. The collection of large amount of data allows a better understanding of the underlying operating principles of such devices, leading to improved design choices.

## References

- [1] D. Webb, H. Zhang, and A. Horwitz, "Cell migration: An overview," *Methods in molecular biology (Clifton, N.J.)*, vol. 294, pp. 3–11, 02 2005.
- [2] N. T. Spratt Jr., "Formation of the primitive streak in the explanted chick blastoderm marked with carbon particles," *Journal of Experimental Zoology*, vol. 103, no. 2, pp. 259–304, 1946.
- [3] J.-F. Bodart, *Embryologie expérimentale : comprendre les mécanismes fondamentaux de l'embryogenèse*. 05 2015.
- [4] D. L. Farkas, C. Du, G. W. Fisher, C. Lau, W. Niu, E. S. Wachman, and R. M. Levenson, "Non-invasive image acquisition and advanced processing in optical bioimaging," *Computerized Medical Imaging and Graphics*, vol. 22, no. 2, pp. 89 – 102, 1998.
- [5] A. S. Arbab, B. Janic, J. L. Haller, E. Pawelczyk, W. Liu, and J. A. Frank, "In vivo cellular imaging for translational medical research.," *Current medical imaging reviews*, vol. 5 1, pp. 19–38, 2009.
- [6] E. Sutton, T. Henning, B. Pichler, C. Bremer, and H. Daldrup-Link, "Cell tracking with optical imaging," *European radiology*, vol. 18, pp. 2021–32, 05 2008.
- [7] A. Stroh, C. Faber, T. Neuberger, P. Lorenz, K. Sieland, P. M. Jakob, A. Webb, H. Pilgrim, R. Schober, E. E. Pohl, and C. Zimmer, "In vivo detection limits of magnetically labeled embryonic stem cells in the rat brain using high-field (17.6 t) magnetic resonance imaging," *NeuroImage*, vol. 24, no. 3, pp. 635 – 645, 2005.
- [8] L. Ferreira, J. M. Karp, L. Nobre, and R. Langer, "New opportunities: The use of nanotechnologies to manipulate and track stem cells," *Cell Stem Cell*, vol. 3, no. 2, pp. 136 – 146, 2008.
- [9] M. Schubert, A. Steude, P. Liehm, N. Kronenberg, M. Karl, E. Campbell, S. Powis, and M. Gather, "Lasing within live cells containing intracellular optical microresonators for barcode-type cell tagging and tracking," *Nano letters*, vol. 15, 07 2015.
- [10] R. Gómez-Martínez, P. Vázquez, M. Duch, A. Muriano, D. Pinacho, N. Sanvicens, F. Sánchez-Baeza, P. Boya, E. J. de la Rosa, J. Esteve, T. Suárez, and J. A. Plaza, "Intracellular silicon chips in living cells," *Small*, vol. 6, no. 4, pp. 499–502, 2010.
- [11] E. Fernandez-Rosas, R. Gómez, E. Ibañez, L. Barrios, M. Duch, J. Esteve, C. Nogués, and J. A. Plaza, "Intracellular polysilicon barcodes for cell tracking," *Small*, vol. 5, no. 21, pp. 2433–2439, 2009.
- [12] P. Rees, J. Wills, M. Brown, J. Tonkin, M. Holton, N. Hondow, A. Brown, R. Brydson, V. Millar, A. Carpenter, and H. Summers, "Nanoparticle vesicle encoding for imaging and tracking cell populations," *Nature methods*, vol. 11, 09 2014.
- [13] C. Guo, W. Kong, K. Kamimoto, G. Rivera-Gonzalez, X. Yang, Y. Kirita, and S. Morris, "Celltag indexing: Genetic barcode-based sample multiplexing for single-cell genomics," *Genome Biology*, vol. 20, p. 90, 05 2019.

- [14] P. Masuzzo, M. V. Troys, C. Ampe, and L. Martens, "Taking aim at moving targets in computational cell migration," *Trends in Cell Biology*, vol. 26, no. 2, pp. 88 – 110, 2016.
- [15] C.-M. Svensson, A. Medyukhina, I. Belyaev, N. Al-Zaben, and M. T. Figge, "Untangling cell tracks: Quantifying cell migration by time lapse image data analysis," *Cytometry Part A*, vol. 93, no. 3, pp. 357–370, 2018.
- [16] J. Sapudom, J. Waschke, K. Franke, M. Hlawitschka, and T. Pompe, "Quantitative label-free single cell tracking in 3d biomimetic matrices," *Scientific Reports*, vol. 7, p. 14135, 10 2017.
- [17] X. Hu, K. Aggarwal, M. X. Yang, K. B. Parizi, X. Xu, D. Akin, A. S. Y. Poon, and H.-S. P. Wong, "Micrometer-scale magnetic-resonance-coupled radio-frequency identification and transceivers for wireless sensors in cells," *Phys. Rev. Applied*, vol. 8, p. 014031, Jul 2017.
- [18] M. Kircher, S. Gambhir, and J. Grimm, "Noninvasive cell-tracking methods," *Nature reviews. Clinical oncology*, vol. 8, pp. 677–88, 09 2011.
- [19] M. Faizan, "Nanoelectromechanical systems for intracellular measurements,"
- [20] J. Zou, V. Yantchev, F. Iliev, V. Plessky, S. Samadian, R. B. Hammond, and P. J. Turner, "Ultra-large-coupling and spurious-free sh0 plate acoustic wave resonators based on thin linbo3," *IEEE Transactions on Ultrasonics, Ferroelectrics, and Frequency Control*, vol. 67, no. 2, pp. 374–386, 2020.
- [21] M. Faizan and L. G. Villanueva, "Frequency-scalable fabrication process flow for lithium niobate based lamb wave resonators," *Journal of Micromechanics and Microengineering*, vol. 30, p. 015008, dec 2019.
- [22] V. Plessky, S. Yandrapalli, P. J. Turner, L. G. Villanueva, J. Koskela, and R. B. Hammond, "5 ghz laterally-excited bulk-wave resonators (xbars) based on thin platelets of lithium niobate," *Electronics Letters*, vol. 55, no. 2, pp. 98–+, 2019.
- [23] P. J. Turner, B. Garcia, V. Yantchev, G. Dyer, S. Yandrapalli, L. G. Villanueva, R. B. Hammond, and V. Plessky, "5 ghz band n79 wideband microacoustic filter using thin lithium niobate membrane," *Electronics Letters*, vol. 55, no. 17, pp. 942–943, 2019.
- [24] A. Lozzi, A. De Pastina, E. T.-T. Yen, and L. G. Villanueva, "Engineered acoustic mismatch for anchor loss control in contour mode resonators," *Applied Physics Letters*, vol. 114, no. 10, p. 103502, 2019.
- [25] S. Gong, *Lithium Niobate for M/NEMS Resonators*, pp. 99–129. 01 2017.
- [26] C. Roth, "Fem modelisation of lamb resonators," June 2019.
- [27] V. Thommen, "Fem modelling of lamb wave resonators," January 2020.
- [28] D. Bindel and S. Govindjee, "Elastic pmls for resonator anchor loss simulation," *International Journal for Numerical Methods in Engineering*, vol. 64, pp. 789 – 818, 10 2005.

- [29] "Comsol multiphysics mems module documentation,"
- [30] J. Zou, "High-performance aluminum nitride lamb wave resonators for rf front-end technology," *PhD Thesis*, 2015.
- [31] M. Germano, A. Alippi, A. Bettucci, and G. Mancuso, "Anomalous and negative reflection of lamb waves in mode conversion," *Physical Review B*, vol. 85, pp. 12102–, 01 2012.
- [32] F. V. Pop, A. S. Kochhar, G. Vidal-Alvarez, and G. Piazza, "Laterally vibrating lithium niobate mems resonators with 30coefficient," in *2017 IEEE 30th International Conference on Micro Electro Mechanical Systems (MEMS)*, pp. 966–969, 2017.
- [33] "Comsol multiphysics reference manual v5.4," 2018.

## 6 APPENDIX

### A Matlab Functions for Data Analysis

Here we present the functions that were implemented in matlab to organize the data obtained from multiple sweeps in COMSOL and obtain values of Quality Factor, Electromechanical Coupling and Resonance Frequency. We also adapted a MATLAB code previously used in the laboratory [26] to identify the SH0 mode shape, in a MATLAB function which can be used on large data sets to automatize the process.

#### A.1 Matlab function for data collection from COMSOL

We use two functions to open and organize the data obtained from COMSOL simulations. The function *openfile*, just converts the *.txt* file into a matrix in matlab containing all the data points. In the case of multiple parametric sweeps, the obtained matrix is then inputted in the function *DataCollection*, that organizes the data in a cell where each cell unit contains a 2 column matrix with admittance and frequency corresponding to a specific combination of the parametric sweep.

##### A.1.1 Function to open COMSOL file

The input and output parameters are:

- **filename**: the location of the text file containing the 2D plotted data (i.e. Admittance vs Frequency) from the COMSOL file. When saving in COMSOL need to de-select from Export Plot Settings the Include Header tab (*Settings > Advanced > Include Header*)
- **Admittance**: a 2D matrix containing all the data points from the text file

The obtained matrix is the same not processed data from the text file obtained in COMSOL and the data will be organized in the following functions.

```
1 function [Admittance] = openfile (filename)
2
3 fid = fopen(filename);
4 Adm = textscan(fid, '%f%f%f', 'MultipleDelimsAsOne', true, 'Delimiter', ';' )
5 ;
6 fclose(fid);
7 Admittance = [Adm{1,1}, Adm{1,2}];
```

##### A.1.2 Function to organize the COMSOL file into a 2D cell

The inputs of the function are the simulation parameters from the study, such as the length of the first and second parametric sweep and an array containing the frequency range (i.e. from 1930 to 1940 MHz with a step of 0.02 MHz would be inputted in the function as [1930, 0.02, 1940]). In the case that

have just one parametric sweep then size\_sweep2 can be set to 1. In the case that have more than two parametric sweeps the function can be modified to include all the parametric sweeps. Note that the output cell obtained in this function will serve as input to function B.2 and B.4.

```

1 function [DataCell] = DataCollection(Admittance, size_sweep1, size_sweep2,
   RANGE)
2
3 N_POINTS = (RANGE(3)-RANGE(1))/RANGE(2) +1;
4
5 last_point=1;
6 data_points_Matrix = zeros(N_POINTS,2);
7 DataCell = cell(size_sweep1, size_sweep2);
8
9 for i=1:1:size_sweep1
10     for j=1:1:size_sweep2
11
12         for x=1:1:N_POINTS
13
14             data_points_Matrix(x,:) = Admittance(last_point,:);
15             last_point=last_point+1;
16
17         end
18
19         DataCell{i,j}=data_points_Matrix;
20
21     end
22 end

```

### A.1.3 Function to open a Table obtained from COMSOL

```

1 function [Table]= opentable(filename, N_Parameters, N_GlobalEvaluations)
2
3 fid = fopen(filename);
4 TableIN = textscan(fid, '%f%f%f%f%f%f%f', 'MultipleDelimsAsOne', true, '
   Delimiter', '[';');
5 fclose(fid);
6
7 Ntot = N_Parameters + N_GlobalEvaluations;
8
9 switch Ntot
10     case 3
11         Table = [TableIN{1,1}, TableIN{1,2}, TableIN{1,3}];
12     case 4
13         Table = [TableIN{1,1}, TableIN{1,2}, TableIN{1,3}, TableIN{1,4}];
14     case 5
15         Table = [TableIN{1,1}, TableIN{1,2}, TableIN{1,3}, TableIN{1,4},
16                 TableIN{1,5}];
17     case 6

```



```

17     Table = [TableIN{1,1}, TableIN{1,2}, TableIN{1,3}, TableIN{1,4},
18             TableIN{1,5}, TableIN{1,6}];
19     case 7
20         Table = [TableIN{1,1}, TableIN{1,2}, TableIN{1,3}, TableIN{1,4},
21                 TableIN{1,5}, TableIN{1,6}, TableIN{1,7}];
22     case 8
23         Table = [TableIN{1,1}, TableIN{1,2}, TableIN{1,3}, TableIN{1,4},
24                 TableIN{1,5}, TableIN{1,6}, TableIN{1,7}, TableIN{1,8}];
25     otherwise
26         disp('too many parameters swept, MODIFY FUNCTION!')
27 end
28 Table = real(Table); % output only real values
end

```

## A.2 Functions for Frequency Domain Studies

### A.2.1 Quality Factor

This function returns the Quality Factor and Resonance frequency from a refined frequency sweep around resonance. The function takes as input the Data cell obtained from function B.1.2 and the length of the first and second parametric sweep. As explained in section 3.2.2 the QF is computed using the FWHM, therefore we need to ensure that the sweep includes the frequency at -3dB from resonance. If this is not the case the function will return a QF of zero and display an error message. Furthermore, to have an accurate result we need to ensure to have enough points within the FWHM as discussed in 3.2.

```

1 function [QF, RF] = QualityFactor(DataCell, size_sweep1, size_sweep2)
2
3 RF = zeros (size_sweep1, size_sweep2);
4 QF = zeros (size_sweep1, size_sweep2);
5 idx = zeros (1,4);
6
7 for i=1:1:size_sweep1
8     for j=1:1:size_sweep2
9
10        Resonance_Matrix = DataCell{i,j};
11
12        resonance_adm = max(Resonance_Matrix(:,2));
13        resonance_index = (Resonance_Matrix(:,2)==resonance_adm);
14        resonance_f = Resonance_Matrix(resonance_index,1);
15        RF(i,j) = resonance_f;
16
17        adm_3dB = resonance_adm -3;
18
19        MIN_VAL = abs(Resonance_Matrix(:,2)-adm_3dB);
20        Ascend_MATRIX = sort(MIN_VAL, 'ascend');
21

```

```

22     % take the first four values of the matrix
23
24     Val = Ascend_MATRIX(1:2);
25     search = [adm_3dB+Val; adm_3dB-Val];
26
27     idx1=find(search(1)==Resonance_Matrix(:,2));
28     idx2=find(search(2)==Resonance_Matrix(:,2));
29     idx3=find(search(3)==Resonance_Matrix(:,2));
30     idx4=find(search(4)==Resonance_Matrix(:,2));
31
32     idx = [idx1, idx2, idx3, idx4] % will return just 2 values
33
34     f_3dB_1 = Resonance_Matrix(idx(1),1);
35     f_3dB_2 = Resonance_Matrix(idx(2),1);
36
37     f_3dB = [f_3dB_1, f_3dB_2];
38     f_3dB_Ascend = sort(f_3dB, 'ascend');
39
40     % sanity check
41
42     if resonance_f > f_3dB_Ascend(1) && resonance_f < f_3dB_Ascend(2)
43
44         DELTA = abs(f_3dB_2 - f_3dB_1);
45         QF(i,j) = resonance_f / DELTA;
46
47     else
48         disp('error')
49         QF(i,j) = 0;
50     end
51
52     end
53 end

```

## A.2.2 Electromechanical Coupling

The function takes as input the Data cell and computes the electromechanical coupling by finding the minimum and maximum admittance, to find the resonance and antiresonance peak, used to calculate  $kt^2$ .

```

1 function [kt, RF] = kt_2(DataCell, size_sweep1, size_sweep2)
2
3 kt = zeros(size_sweep1, size_sweep2);
4 RF = zeros(size_sweep1, size_sweep2);
5 for i=1:1:size_sweep1
6     for j=1:1:size_sweep2
7         %for k=1:1:size_sweep3
8
9         Matrix_Adm = DataCell{i,j};
10

```

```

11     % calculate resonance f and kt^2
12
13     adm_r=max(Matrix_Adm(:,2));
14     adm_ar = min(Matrix_Adm(:,2));
15
16     f_r = Matrix_Adm(Matrix_Adm(:,2)==adm_r,1);
17     f_ar=Matrix_Adm(Matrix_Adm(:,2)==adm_ar,1);
18     kt(i,j)=100*((pi^2)/4)*(f_ar-f_r)/f_ar;
19     RF(i,j)=f_r;
20     % end
21 end
22 end

```

### A.3 QF from Modal Analysis

The codes presented in this section, were re-adapted from [26] into MATLAB functions.

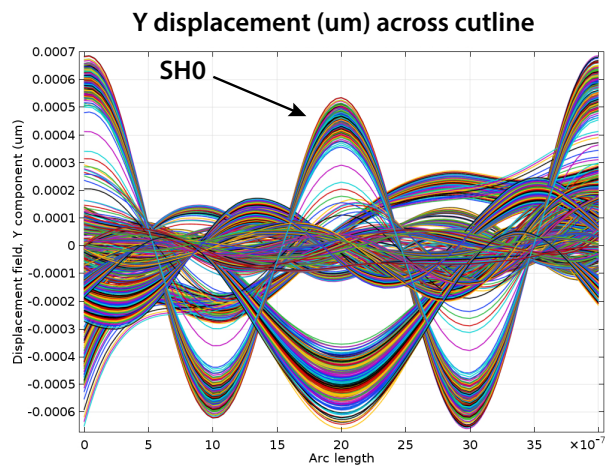
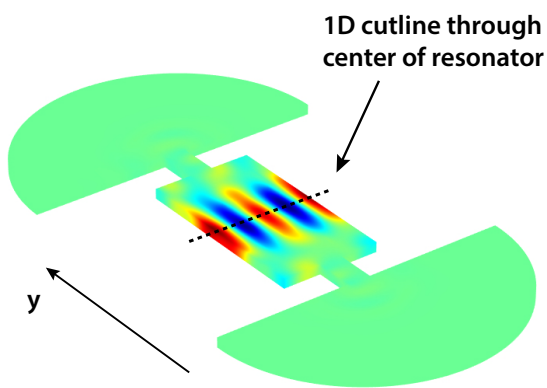


Figure 16

#### A.3.1 Mode Identification

```

1 function [Boolean_MODE_ID]= ModeID(Ydisplacement, Nfingers, threshold)
2
3 % Ydisplacement is obtained using the function openfile
4
5 index = find(Ydisplacement(:,1) == 0);
6 s = length(index);
7 CellDP = cell(s, 1);
8 normalizedpeaks = cell(s,1);
9 mean_peaks = zeros(s,1);
10 peaks_length = zeros(s,1);

```

```

11 Boolean_MODE_ID = zeros(s,1);
12 peaks = cell(s,1);
13
14 for i = 1:s-1
15     CellDP{i,1} = Ydisplacement(index(i):1:(index(i+1))-1, :);
16 end
17
18 CellDP{s,1} = Ydisplacement(index(s):end,:);
19
20 for x = 1:1:s
21     YD_MODE = CellDP{x};
22     YD_MODE_ABS = abs(YD_MODE(:,2));
23     peaks{x} = findpeaks(YD_MODE_ABS);
24     mean_peaks(x,1) = mean(peaks{x}); % Mean value for all peaks
25     peaks_length(x,1) = length(peaks{x}); % Number of peaks
26     clear YD_MODE;
27     clear YD_MODE_ABS;
28 end
29
30 % substitute the values NaN in mean_peaks with 0
31 idx_NaN = isnan(mean_peaks);
32 mean_peaks(idx_NaN) = 0;
33 mean_all_peaks = mean(mean_peaks);
34
35 for i = 1:s
36     normalizedpeaks{i} = peaks{i} ./ mean_all_peaks;
37 end
38
39 % Selection of SH0 Mode
40 for i = 1:s
41     if peaks_length(i) ~=(Nfingers-1)
42         Boolean_MODE_ID(i) = 0;
43     elseif all(normalizedpeaks{i} > threshold)
44         Boolean_MODE_ID(i) = 1;
45     else
46         Boolean_MODE_ID(i) = 0;
47     end
48 end
49
50 end

```

### A.3.2 QF Eigenfrequency for 3D Plots

```

1 function [X, Y, QF, RF] = QFModal(param1, param2, colP1, colP2, columnQF,
2     columnRF, Table)
3
4 RF = zeros(length(param1), length(param2));
5 QF = zeros(length(param1), length(param2));
6 X = repmat(param1', 1, length(param2));
7 Y = repmat(param2, length(param1), 1);

```

```

7
8 for i= 1:1:size(X,1)
9     for j=1:1:size(X,2)
10
11         row = find(Table(:,colP1)==Y(i,j)& Table(:,colP2)==X(i,j));
12         if isempty(row)
13             QF(i,j)=NaN;
14             RF(i,j)=NaN;
15
16         elseif length(row)>1
17             QF(i,j)=NaN;
18             RF(i,j)=NaN;
19
20         else
21             QF(i,j)= Table(row, columnQF);
22             RF(i,j)= Table(row, columnRF);
23
24         end
25     end
26 end
27
28 figure()
29 surf(X,Y, QF, 'FaceAlpha',0.7,'EdgeColor','interp', 'LineWidth',1, '
30     FaceColor', 'interp')
31 colormap(jet)
32
33 figure()
34 surf(X,Y, RF, 'FaceAlpha',0.7,'EdgeColor','interp', 'LineWidth',1, '
35     FaceColor', 'interp')
36 colormap(jet)
37 end

```